Coaxial mode excitation and dissipation in ion Bernstein wave experiments

J.R. Myra and D.A. D'Ippolito and D.A. Russell

Lodestar Research Corporation, Boulder Colorado

J.H. Rogers

Princeton Plasma Physics Laboratory, Princeton, NJ

T. Intrator,

University of Wisconsin - Madison, Madison, WI

December 1998

(submitted to Physics of Plasmas)

DOE/ER/54212-4 LRC-97-66

LODESTAR RESEARCH CORPORATION

2400 Central Avenue

Boulder, Colorado 80301

Coaxial mode excitation and dissipation in ion Bernstein wave experiments

J.R. Myra, D.A. D'Ippolito and D.A. Russell,

Lodestar Research Corporation, Boulder CO

J.H. Rogers†

Princeton Plasma Physics Laboratory, Princeton, NJ

T. Intrator,

University of Wisconsin - Madison, Madison, WI

In recent ion Bernstein wave (IBW) heating experiments on the Tokamak Fusion Test Reactor (TFTR) [1] a velocity shear layer in the plasma core was obtained. The magnitude of velocity shear was believed to be too small to create an internal transport barrier because of parasitic edge processes which reduced the power coupled to the core. In this paper we investigate these rf edge processes by employing a model which includes both coaxial modes and their dissipation in rf plasma sheaths. The coaxial mode (here, an electron plasma wave trapped in the halo plasma between the lower hybrid layer and the vessel wall) can propagate at low poloidal wavenumbers. This feature is shown to relate to the observed poloidal phasing dependence of the antenna loading. Results of analytical models and a three dimensional antenna code are presented. The experimentally observed loading is also nonlinear, being larger at very low powers. This feature is explored using an rf sheath dissipation model. Loading into the coaxial mode is expected to maximize when the density gradient at the lower hybrid layer is steep, preventing efficient mode transformation to the IBW. The role of ponderomotive force in modifying the density profile is also discussed.

† present address: Intevac, Inc., Santa Clara, California

PACS numbers: 52.50.Gj, 52.40.Hf, 52.40.Fd, 52.55.Fa

I. Introduction

The possibility of employing the ion Bernstein wave (IBW) to heat fusion plasmas has long been regarded as fundamentally attractive because the IBW is efficiently absorbed by hot ions or electrons and can directly heat the thermal particle distribution of the main species if desired. There is a considerable literature on both the experimental and theoretical aspects of the launch, propagation and absorption of the IBW.[1-5] Recently, it has been pointed out theoretically[4] and shown experimentally[5] that the IBW could be employed to generate a velocity shear layer in the plasma, and thereby induce a transport barrier. These results have strongly motivated recent attempts to better understand IBW physics.

From a theoretical standpoint, the IBW is characterized by: (i) its short wavelength, which requires a treatment of finite Larmor radius effects; (ii) a slow group velocity, which usually means electric field amplitudes must be large (and frequently nonlinear) to transmit interesting levels of power; and, (iii) a polarization that results in both radial and parallel (along B) electric fields, and therefore substantial rf sheath voltages[6] driven by the parallel component.

The IBW has been successfully launched in a number of small experiments, but it has generally been found to be difficult to couple significant power to the core plasma using IBW in large tokamaks. This failure in large machines may be related to larger plasma - wall distances and higher plasma density, both of which increase the likelihood of coaxial mode (CM) propagation. These coaxial modes, and their relevance to recent experiments on the Tokamak Fusion Test Reactor[1] (TFTR) are the subject of the present paper.

In recent IBW heating experiments on TFTR[1,2] a velocity shear layer in the plasma core was obtained. The magnitude of velocity shear was too small to create an internal transport barrier, possibly because of parasitic edge processes which reduced the power coupled to the core, P_{core}. However, the successful formation of an IBW-induced shear layer is an exciting result, and motivates the present work directed towards understanding

and improving upon these experiments. The experimental observations of relevance to the present work are as follows:

- $P_{core}/P_{rf} << 1$ in 0-0-0-0 phasing,
- R_L depends on poloidal phasing with higher loading in 0-0-0-0 phasing,
- R_L depends on P_{rf}, hence some nonlinear processes are at work.

Here, P_{rf} is the total rf power delivered by antenna and R_L is the loading resistance. In this paper, we investigate candidate rf edge processes by employing models which describe the excitation and dissipation of the coaxial mode.

The meaning of the terminology "coaxial mode" as employed herein is an electron plasma wave (EPW) trapped in the halo plasma between the lower hybrid (LH) layer and the vessel wall. In the simplest approximation of an electrostatic mode in slab geometry propagating in a uniform density plasma, the dispersion relation for the CM is

$$k_x^2 = -k_y^2 + \frac{k_\parallel^2 \omega_{pe}^2}{\varepsilon_\perp \omega^2} \qquad (1)$$

where (x, y, z) denote the (radial, poloidal, toroidal) directions. In the low density halo plasma $\varepsilon_\perp \approx 1$, and the mode propagates in x for sufficiently small k_y. Above the LH resonance $\varepsilon_\perp < 0$, and the mode is evanescent. (In a model with finite Larmor radius, the mode transforms to the IBW as it propagates through the LH layer.[3]) Loading into the coaxial mode is expected to maximize when the density gradient at the LH layer is steep, enhancing reflections and preventing efficient mode transformation to the IBW. This feature and the role of ponderomotive steepening and induced reflection have been treated elsewhere.[7]

The TFTR experimental observation that loading depends on poloidal (y) phasing (0-0-0-0 or 0-0-π-π) is suggestive of the notion that the CM propagates only at low k_y. In this paper, we explore this dependence and the dependence of the power split P_{out}/P_{rf} on dissipation in the halo plasma, where $P_{out} = P_{rf} - P_{halo}$. An explanation of the observed dependence of R_L on P_{rf} requires nonlinear physics. Here we investigate two possibilities:

sheath dissipation due to halo and scrape-off layer (SOL) sheaths, and the nonlinear dependence introduced by the ponderomotive steepening itself.

The plan of our paper is as follows. Experimental data motivating this paper is presented in Sec. II. In Sec. III. we present models for the halo plasma, slow wave fields and antenna impedance. Three coaxial mode models are presented in Sec. IV, together with numerical results for the loading in a "sharp boundary" density model. In Sec. V, we consider diffuse density profile calculations with self-consistent ponderomotive force. Sec. VI contains the results of more sophisticated three-dimensional electromagnetic antenna modeling which remove some of the assumptions necessary in the analytical work of Secs III - V. A discussion and summary is given in Sec. VII. Finally, some details of the analytic models are given in the appendices.

II. Experimental Motivation

As mentioned in the introduction, the motivation for the present work comes from direct launch IBW experiments conducted on TFTR. Some of the experimental results have been reported in Refs. 1 and 2, to which we refer the reader for a more detailed description of the experiments.

The models to be presented herein relate to the observed phasing and power dependence of the loading. The dependencies are illustrated in Figs. 1 and 2. Figure 1 (taken from Ref. 2) shows TFTR data for antenna loading R_L vs. the antenna position $R_{antenna}$ for 0-0-0-0 and 0-0-π-π poloidal phasing. The 0-0-0-0 phasing data includes ohmic and neutral beam targets, and various plasma sizes (2.58 m < R_p < 2.61 m), with B_0 = 4.7 T and B_0 = 3.6 T. The 0-0-π-π phasing data is for ohmic target plasmas with R_p = 2.61 m and B_0 = 2.4 T. The main point to note here is that the loading is about a factor of two to three higher in 0-0-0-0 phasing.

Figure 2 shows TFTR data for R_L vs. P_{rf} in 0-0-π-π poloidal phasing. The target was an ohmic plasma, with B_0 = 2.4 T. The loading is a decreasing function of power,

being about a factor of 2 higher at 1 kW than at 1 MW, and indicates that some nonlinear mechanism is operative.

These figures represent only a small portion of the TFTR IBW dataset, but are a useful focus for the theoretical analysis which follows.

III. Halo plasma, slow wave and antenna loading models

A. Fundamental equations

Starting from the Fourier transformed wave equation

$$(\mathbf{nn} - n^2 \mathsf{I} + \varepsilon)\cdot\mathbf{E} = -(4\pi i/\omega)\,\mathbf{J}_a \qquad (2)$$

where $\mathbf{E}$ is the electric field, $\mathbf{n} = \mathbf{k}c/\omega$ with $\mathbf{k}$ the wavevector and ω the frequency, ε is the dielectric tensor, and $\mathbf{J}_a$ is the antenna current, we focus on the slow wave (SW) branch. Here and elsewhere in this paper, theoretical derivations are presented in the CGS system of units. The SW is characterized by two components of E, one in the direction of $\mathbf{k}_\perp$, and the other parallel to the equilibrium magnetic field $\mathbf{B}$, and has $n_\perp^2 >> 1$, $\varepsilon_\perp$, $n_\parallel^2$. Here, the dielectric tensor is given by $\varepsilon = (\mathsf{I}-\mathbf{bb})\varepsilon_\perp + \mathbf{bb}\varepsilon_\parallel$, with $\varepsilon_\perp = 1 - \omega_{pi}^2/(\omega^2-\Omega_i^2)$ and $\varepsilon_\parallel = 1 - \omega_{pe}^2/\omega^2$. In the SW ordering, the off-diagonal terms of ε may be neglected. Thus the following 2×2 set of equations results:

$$\begin{pmatrix} \varepsilon_\perp - n_\parallel^2 & n_\perp n_\parallel \\ n_\perp n_\parallel & \varepsilon_\parallel - n_\perp^2 \end{pmatrix} \begin{pmatrix} E_\perp \\ E_\parallel \end{pmatrix} = -\frac{4\pi i}{\omega} \begin{pmatrix} J_{a\perp} \\ J_{a\parallel} \end{pmatrix}$$

Introducing the scalar and vector potentials Φ, $\mathbf{A}$ in the Coulomb gauge ($\mathbf{k}\cdot\mathbf{A} = 0$) and taking $\mathbf{E}_\perp = -\nabla\Phi + i\omega A_\perp/c \rightarrow -ik_\perp\Phi - k_\parallel a_\parallel/k_\perp$, $\mathbf{E}_\parallel = -\nabla_\parallel\Phi + i\omega A_\parallel/c \rightarrow -ik_\parallel\Phi + a_\parallel$ where $a_\parallel = i\omega A_\parallel/c$ and all wave quantities vary as $\exp(-i\omega t + i\mathbf{k}\cdot\mathbf{x})$, we obtain coupled equations for Φ and $a_\parallel$

$$k_\perp^2\,\varepsilon_\perp\Phi + k_\parallel^2\,\varepsilon_\parallel\Phi + ik_\parallel\varepsilon_\parallel a_\parallel = -(4\pi i/\omega)\nabla\cdot\mathbf{J}_a, \qquad (3)$$

$$(\varepsilon_\parallel - n_\perp^2)a_\parallel - i\varepsilon_\parallel k_\parallel\Phi = -(4\pi i/\omega)J_{a\parallel}. \qquad (4)$$

In obtaining Eqs. (3) and (4) we have made use of the SW ordering $\varepsilon_\perp \sim n_\parallel^2 << \varepsilon_\parallel \sim n_\perp^2$ to drop some small terms. Eliminating $a_\parallel$ results in

$$n_\perp^2(n_\perp^2\varepsilon_\perp + n_\parallel^2\varepsilon_\parallel - \varepsilon_\perp\varepsilon_\parallel)\Phi = (4\pi i c^2/\omega^3)(\varepsilon_\parallel - n_\perp^2)\nabla\cdot\mathbf{J}_a + (4\pi n_\parallel c\varepsilon_\parallel/\omega^2)J_{a\parallel} \qquad (5)$$

The two factors on the left-hand side correspond to the fast wave in the present approximation ($n_\perp^2 = 0$) and the SW. The desired reduced second order equation for the SW branch is obtained by retaining only the SW pole, i.e. dividing through by $n_\perp^2$ and evaluating it in the source term from the SW dispersion relation

$$n_\perp^2\varepsilon_\perp + n_\parallel^2\varepsilon_\parallel - \varepsilon_\perp\varepsilon_\parallel = 0. \qquad (6)$$

This procedure results in the equation

$$(n_\perp^2\varepsilon_\perp + n_\parallel^2\varepsilon_\parallel - \varepsilon_\perp\varepsilon_\parallel)\Phi = \frac{4\pi c n_\parallel}{\omega^2(n_\parallel^2 - \varepsilon_\perp)}(n_\parallel \mathbf{n}\cdot\mathbf{J}_a - \varepsilon_\perp J_{az}) \qquad (7)$$

$$= \frac{4\pi c n_\parallel}{\omega^2}\left(J_{az} + \frac{n_\parallel n_x}{(n_\parallel^2 - \varepsilon_\perp)}J_{ax}\right)$$

where two forms for the source terms have been given, with $J_{a\parallel} = J_{az}$ and $J_{a\perp} = J_{ax}$.

B. Model geometry

We wish to solve Eq. (7) in the model geometry of Fig. 3. In the figure, the main (core + SOL) plasma is to the left of x = 0 (not modeled here), and x = g represents the back wall of the antenna and vacuum vessel. Thus we model the antenna and halo plasma region *outside* the LH layer. It is important to emphasize that many phenomena in the SOL and edge plasma can influence the waves between their launch from the antenna, and their eventual absorption. Here, we model only processes that occur in the halo plasma. A constant density is assumed in this region both for simplicity, and because experimental measurements of the profile are not available. It is possible to make one of two approximations for the antenna model: either $J_{ax} = 0$ (neglect of feeders), or $\mathbf{n}\cdot\mathbf{J}_a = 0$ (purely inductive coupling). To describe these two limits we introduce the parameter G, and integrate Eq. (7) across the current strap (converting $k_\perp \rightarrow -i\partial/\partial x$) to obtain the jump condition

$$\left[\frac{\partial\Phi}{\partial x}\right]_-^+ = \frac{4\pi I_k n_\parallel G}{c L_y(n_\parallel^2 - \varepsilon_\perp)}, \qquad (8)$$

where $G = (\varepsilon_\perp - n_\parallel^2)/\varepsilon_\perp$ in the $J_{ax} = 0$ approximation, and $G = 1$ in the inductive $\mathbf{n}\cdot\mathbf{J}_a = 0$ approximation. Here we have taken the antenna current density to be $J_{az} = I_k\, \delta(x-a) / L_y$, where $I_k = iI_0\, [\exp(-ik_\parallel L_z) - 1]/k_\parallel$ is the Fourier transform of a current of magnitude I_0 in the z direction, that is constant between the "feeder" locations at $z = 0$ and $z = L_z$ and zero elsewhere and has poloidal width L_y.

The description of the model is completed by specifying the boundary conditions (BCs). At the back wall, $x = g$, we take the conducting BC

$$\Phi = 0. \tag{9a}$$

At the LH layer, $x = 0$, we wish to describe partial transmission/reflection of the waves. This is accomplished by demanding that Φ have the form

$$\Phi = A\, [\exp(ikx) + \alpha \exp(-ikx)] \tag{9b}$$

in region 1, where α is an input parameter equal to 0 for pure outgoing wave BC's and equal to -1 for a pure standing wave (conducting boundary at $x = 0$). We note that the EPW is a "backward propagating mode" [see Eq. (1) or (6)], i.e. one with phase and group velocities in the opposite direction, so the phase factor $\exp(ikx)$ represents *left*-going wave energy.

C. Antenna impedance and sheath driving voltage

It is straightforward to solve Eqs. (7) - (9); the result is

$$\Phi = \begin{cases} A[\exp(ikx) + \alpha \exp(-ikx)], & 0 < x < a \\ \\ B \sin k(x - g), & a < x < g \end{cases} \tag{10}$$

$$A = \frac{-4\pi I_k n_\parallel G}{cL_y(n_\parallel^2 - \varepsilon_\perp)k[\exp(ika) + \alpha \exp(-ika)][\cot(ks) + iQ]}, \tag{11}$$

$$B = \frac{-A[\exp(ika) + \alpha \exp(-ika)]}{\sin(ks)}, \tag{12}$$

$$Q = \frac{\exp(ika) - \alpha \exp(-ika)}{\exp(ika) + \alpha \exp(-ika)}. \tag{13}$$

Hence, the potential Φ_{ka} and current I_k at the location of the current strap are related by

$$\frac{\Phi_{ka}}{I_k} = \frac{-4\pi n_{||} G}{cL_y(n_{||}^2-\varepsilon_\perp)k[\cot(ks)+iQ]} . \tag{14}$$

In the above expressions, k is shorthand notation for k_x which is to be obtained as a function of k_y (an input parameter to the model) and $k_z = k_{||}$ from the dispersion relation, Eq. (6).

Having the solution at hand, the model yields an analytical expression for the antenna impedance

$$Z = \frac{1}{I_0}\int_0^{L_z} dz\, E_{za} = \frac{1}{I_0^2}\int \frac{dk_{||}}{2\pi} I_k^*\, E_{za}(k_{||}), \tag{15}$$

which can also be written in the form

$$Z = \int \frac{dk_{||}}{2\pi} \frac{2i}{k_{||}} [1-\cos(k_{||}L_z)] \frac{n_\perp^2\varepsilon_\perp}{n_{||}^2\varepsilon_{||}} \frac{\Phi_{ka}}{I_k}, \tag{16}$$

In the present analysis, it is useful (but not essential) to simplify the results by (i) taking $\varepsilon_\perp = 1$ in the very low density halo plasma, and (ii) passing to the limit $n_{||}^2 >> 1$, which is well satisfied for the main portion of the antenna spectrum. In this case, Eq. (16) reduces to

$$Z = \frac{-i}{\pi}\int \frac{dk_{||}}{k_{||}} [1-\cos(k_{||}L_z)] \frac{\Phi_{ka}}{I_k}, \tag{17}$$

and upon using the explicit solution for Φ_{ka} we obtain

$$Z = \frac{4i\omega}{c^2L_y}\int \frac{dk_{||}}{k_{||}^2} \frac{[1-\cos(k_{||}L_z)]G}{k[\cot(ks)+iQ]}. \tag{18}$$

We note that Q = 1 for pure outgoing waves, and Q =i cot(ka) for pure standing waves. The physical meaning of the two limiting cases for G is now apparent. To illustrate this we consider the case of no dissipative losses (Q pure imaginary) and vacuum dispersion. In the $\mathbf{n}\cdot\mathbf{J}_a = 0$ limit, G = 1, Eq. (18) gives $Z \propto -i\omega L$ for some inductance L, while the opposite case with $J_{ax} = 0$, $G \approx -n_{||}^2$, gives $Z \propto i/\omega C$ for some capacitance C, thus the two limits correspond to inductive and capacitive coupling respectively. We work in the inductive limit henceforth because it is more representative of the experimental coupling,

and because the Faraday shield, not explicitly modeled here, is designed to screen out the capacitive coupling. A more general treatment of the coupling, including both inductive and capacative effects, is given in Sec. VI where the results from three-dimensional electromagnetic antenna modeling are presented.

The pole at cot(ks)+iQ = 0 in Eq. (18) describes the CM. For example, in the limit $\alpha = -1$, the pole is on the real axis and results in the condition $kg = m\pi$ (m = 1, 2, 3 ...) which are the standing wave eigenmodes.

The model also allows analytical calculation of the induced voltage along a field line which is available for driving rf sheaths,

$$V_{sh} = \int_{-\infty}^{\infty} dz\ E_z\ , \tag{19}$$

and the corresponding sheath power dissipation[8,9]

$$P_{sh} = n_e e c_s A \langle V_{sh} \rangle . \tag{20}$$

Here, the integral is taken on the infinite domain for mathematical convenience, and <> represents a suitable radial average to be defined in Sec. IV. In Eq. (20), n_e is the electron density, e the electron charge, c_s the sound speed and A the sheath area in the x-y plane. Rf sheaths are expected to form on field lines passing in front of the antenna that contact conducting surfaces such as limiters which can complete the sheath circuit.

IV. Numerical results for three coaxial mode models

In this section, we consider three models for the coaxial mode, each of which emphasizes different physics relevant to the experimental observations.

A. Model 1: no dissipation of the CM

The simplest situation is when there is no dissipation of the CM, corresponding for example to the dispersion relation of Eq. (1). The loading power $P_{load} = I_0^2 R_L / 2$, where $R_L = Re(Z)$, can be cast into the form

$$\frac{R_L}{Z_0} = (1-\alpha^2)\, f_{out}, \tag{21}$$

where Z_0 is a characteristic value of the impedance given by

$$Z_0 = \frac{4\omega L_z g}{L_y c^2}\ , \tag{22}$$

and f_{out} is a dimensionless integral which contains the details of the antenna spectrum,

$$f_{out} = \int_{-\infty}^{\infty} \frac{dk_{||}}{L_z k_{||}^2} \frac{(1-\cos k_{||} L_z)\mathrm{Re}(kg)}{|\exp(ika)+\alpha\exp(-ika)|^2 |\cot(ks)+iQ|^2 |kg|^2}. \tag{23}$$

The main features of this model are illustrated in Figs. 4 - 6. The default parameter choices for the figures of the paper are given in Table 1. Figure 4 shows the normalized loading as a function of k_y for $\alpha = 0$ and -0.9. It can be seen that R_L is a decreasing function of k_y because at large k_y a greater portion of the CM spectrum is radially evanescent. The loading is larger in the case of pure outgoing BCs ($\alpha = 0$) than in the case of mostly reflecting BCs ($\alpha = -0.9$). The general decrease of R_L with k_y is qualitatively consistent with the experimentally observed phasing dependence discussed in Secs. I and II. The details depend on the parameters, of which the halo density is perhaps the most interesting because its value is not known accurately in the experiments. From Eq. (1) it is to be expected that the cutoff condition is determined by both n_e and k_y.

In Fig. 5, the n_e dependence is explored for $k_y g = 0$ and 3 with $\alpha = -0.9$. These values for $k_y g$ approximate the central lobes of the poloidal antenna spectrum in 0-0-0-0 and 0-0-π-π phasing respectively. Several features are apparent. First examining the $k_y = 0$ curve, the first coaxial mode resonance $k_x \sim \pi/g$ occurs near $n_e = 3 \times 10^9$ cm^{-3} and is very broad due to the broad $k_{||}$ spectrum of the antenna. The low density behavior is discussed subsequently. Turning to the $k_y g = 3$ curve, it has lower loading, as also seen in Fig. 4, and the peak occurs at slightly larger n_e because the $-k_y^2$ term in the dispersion relation competes with the positive n_e term. Below $n_e = 10^8$ cm^{-3} essentially all of the spectrum is evanescent, so the loading goes to zero. Comparing the two curves, we see

that a factor of two difference in loading is possible in the range $n_e = 10^9$ to 10^{10} cm^{-3}. This figure employs the model dispersion relation given by Eq. (1) and is therefore not accurate at low densities where the vacuum term in $\varepsilon_{||}$ leads to a plasma wave resonance in the $k_y = 0$ curve at $\omega = \omega_{pe}$ near $n_e \approx 7 \times 10^7$ cm^{-3}; however, as we shall see, such low densities are not of interest for other reasons.

The qualitative results of model 1 are not very sensitive to α, as illustrated in Fig. 6. There is a modest decrease in loading as the tendency towards wave reflection increases.

To summarize the results from model 1, it qualitatively reproduces the observed phasing dependence of the loading for halo densities in the range 10^9 to 10^{10} cm^{-3} and is reasonably insensitive to other parameters, within their brackets of uncertainty. The main difficulty with model 1 is that all the power goes into the outgoing wave; there is no other place for it to be dissipated. This could be consistent with experiment if there were some other dissipation mechanism in the SOL ($x < 0$), outside of the region being modeled, that affected the IBW before it reached the core. (Recall that the waves transmitted to $x < 0$ in this model mode transform to the IBW.) Sheath dissipation of the IBW on the rf limiters, as proposed in Ref. 8 is one possibility; but in the following subsections we explore some other dissipation mechanisms that act directly on the fields in the halo region $x > 0$.

B. Model 2: fixed linear dissipation of the CM

There are various linear dissipation mechanisms which could be operative in the halo plasma; neutral collisions and Landau damping are two possible examples. It is not our intention here to give first principles calculations of a particular dissipation mechanism, but rather to examine whether *any* such mechanism could be consistent with the constraints imposed by the experimental loading and heating efficiency data.

When there is dissipation in the halo, k (i.e. k_x obtained from the relevant dispersion relation) will be complex, and it is expected that the loading power can be split into pieces that represent outgoing power (transmitted to $x < 0$) and power dissipated in the

halo, viz. $P_{load} = P_{out} + P_{halo}$. Model expressions for this power split are obtained in Appendix A. The results can be expressed in the form

$$\frac{R_L}{Z_0} = (1-\alpha^2)\, f_{out} + f_{halo}, \tag{24}$$

$$f_{halo} = \int_{-\infty}^{\infty} \frac{dk_{\|}}{L_z k_{\|}^2} \frac{(1-\cos k_{\|} L_z)}{|\cot(ks)+iQ|^2 |k|^2} \times \left(\frac{h_{halo-}}{ag|\exp(ika)+\alpha \exp(-ika)|^2} + \frac{k_i \sin(2k_r s) - k_r \sinh(2k_i s)}{2g\,|\sin(ks)|^2} \right), \tag{25}$$

$$h_{halo-} = k_r a(1-\alpha^2)[\cosh(2k_i a)-1] - k_r a(1+\alpha^2)\sinh(2k_i a) - 2\alpha k_i a \sin(2k_r a). \tag{26}$$

The two terms in f_{halo} correspond to power flowing to the left and right of the current strap. The power split between f_{out} (the same as in model 1) and f_{halo} is determined by calculating the outgoing power from the Poynting flux at x = 0, and taking P_{halo} to be everything else in the loading integral. Note that when k_i = Im(k) vanishes, so does f_{halo} and P_{halo}. We model the dissipation phenomenologically by taking $k_x = k_{x0} + i\, k_d$ where k_{x0} is the value given by the dispersion relation of Eq. (1), and k_d is an input parameter.

Results for this model are shown in Fig. 7 which gives R_L as a function of k_y for outgoing waves (α = 0) showing the power split between P_{out} and P_{halo}. Note that the loading decreases with k_y for this model, as in model 1, in qualitative agreement with the experiments. Furthermore, the power split f_{halo}/f_{out}, determined by α and k_d can be made large or small, and is substantial for the parameters of this figure.

Thus model 2 reproduces all the desirable features of model 1, but in addition can (with the proper choice of parameters) yield a solution in which only a small fraction of the loading power is delivered to the outgoing wave. The main deficiency of model 2 is that is not obvious how to explain the observed power dependence of the loading: in a linear model, R_L will always be independent of the rf power. It is possible that α could be a

function of power through the ponderomotive force, and we shall return to this idea in Sec. V. Next, however, we consider another possibility.

C. Model 3: sheath dissipation of the CM

In this subsection, for pedagogical simplicity, we set $k_d = 0$, and return to the simpler case of model 1 where k is real. Clearly, both sheath and linear dissipation could coexist. To model sheath dissipation on the rf limiters, we employ Eqs. (19) and (20) to obtain an expression for P_{sh}, and then add this to P_{out} to obtain

$$P_{load} = Z_0 \left[\frac{1}{2} I_0^2(1-\alpha^2)\, f_{out} + I_0 I_{sat}\right] \tag{27}$$

$$\frac{R_L}{Z_0} = (1-\alpha^2)\, f_{out} + \frac{2I_{sat}}{I_0} \tag{28}$$

where for a given power $P_{rf} = P_{load}$, I_0 is determined by solving the quadratic equation, Eq. (27), and this value is then employed to get the loading from Eq. (28). Details of the derivation are given in Appendix B. The important feature of Eq. (27) is that we introduce a power dissipation that is proportional to I_0 in addition to the usual I_0^2 dependence. I_{sat} has the dimensions of the sheath saturation current, and also includes factors which account for the x variation of the sheath voltage $<X_0>$ and its explicit dependence on k_y at the x location of the current strap. Using the solution for Φ in the model geometry, we obtain the results

$$I_{sat} = \frac{\pi}{2} e c_s \frac{n_{ehalo} A <X_0> + n_{etail} <AX_{t0}>}{k_y g[\coth(k_y s) + Q_y]}, \tag{29}$$

$$<X_0> = \frac{[\exp(k_y a) - 1] + \alpha[1 - \exp(-k_y a)]}{k_y g[\exp(k_y a) + \alpha \exp(-k_y a)]} + \frac{\cosh(k_y s) - 1}{k_y g \sinh(k_y s)}, \tag{30}$$

$$<AX_{t0}> = \frac{2\alpha L_y k_y \delta_e^2}{\varepsilon_{\perp s}[\exp(k_y a) + \alpha \exp(k_y a)]}, \tag{31}$$

$$Q_y = \frac{\exp(k_y a) - \alpha \exp(-k_y a)}{\exp(k_y a) + \alpha \exp(-k_y a)}. \tag{32}$$

Here, two types of sheaths have been retained, the sheaths due to the CM in the halo plasma proper given by $n_{ehalo}A<X_0>$, and those due to the evanescent tail of the CM which extends slightly into the region $x < 0$. The latter are given by the $n_{etail}<AX_{t0}>$ term, where n_{etail}, $\delta_e = c/\omega_{pe}$ and $\varepsilon_{\perp s}$ are evaluated in the higher density ($n > n_{lh}$) SOL plasma to the left of $x = 0$ in Fig. 3. Details of the derivation may be found in Appendix B.

Results for this model are illustrated in Figs. 8 and 9. Figure 8 show R_L as a function of P_{rf} for $\alpha = -0.9$ (significant reflection) for the cases $k_y g = 0$ and 3. For each k_y, the upper (solid) curve gives the total loading, and the lower (dashed) curve gives the portion thereof due to sheath power dissipation in the halo and tail. The variation in loading is about a factor of two between 1 kW and 1 MW, in rough agreement with experimental measurements. The rise at low power is due to the I_{sat}/I_0 term in Eq. (28) which becomes dominant at low powers. This effect has previously been noted for low power fast wave loading.[9] The low power enhancement is slightly stronger in 0-0-0-0 phasing than in 0-0-π-π phasing. Results are insensitive to α (not shown).

At one megawatt, the power dissipated in CM halo sheaths is completely negligible because I_{sat} is very small ($<< I_0$), being proportional to the halo density. It is possible that a much more significant fraction of rf power is dissipated in the high density sheaths on the rf limiters that are driven by the IBW itself in the region $x < 0$. This estimate has been given elsewhere,[8] and is outside the scope of the present model. It is worth noting, however, that the power dependence of IBW sheaths may not show the scaling of Fig. 8. The argument is that the IBW in the SOL has a much shorter wavelength and is therefore part of the "far field" of the antenna; thus, the power coupled to the IBW (and any fraction thereof which may be dissipated in sheaths) is included in the outgoing Poynting flux at $x = 0$. The actual loss mechanism for this energy (e.g. core absorption vs. SOL dissipation) would then be irrelevant from the standpoint of the antenna loading. Therefore by this argument any sheath power dissipation of the mode-converted IBW itself would not be expected to contribute to the low-power loading peak seen in Fig. 8.

Figure 9 shows the saturation current I_{sat} as a function of k_y, with the individual contributions of the halo and tail sheaths broken out. The sheath power dissipation is proportional to I_{sat}. For most experimentally relevant values of k_y the tail and halo sheaths give comparable contributions.

To summarize model 3, it has all the desirable features of model 1, but in addition gives loading that is dependent on power. The calculated variation in loading is about a factor of two between 1 kW and 1 MW, in rough agreement with experiment .

V. Diffuse profile calculations with self-consistent ponderomotive force

One of the inadequacies of the previous section is that the parameter α, which describes the amount of reflection from the LH layer, is an input parameter which has not been calculated self-consistently. Furthermore, the analytical model employs a sharp boundary (discontinuous density profile) and does not describe the EPW - IBW mode transformation process. These inadequacies are remedied in the present section, where we employ a diffuse profile code with EPW - IBW mode transformation physics, and self-consistent ponderomotive force and subsequent reflection of the EPW (CM).

The code, which is limited to the $k_y = 0$ case, has been described in detail elsewhere.[7] In this code, the CM geometry is a bit different than in Sec. IV because a vacuum region rather than a low density halo plasma is assumed beyond the Faraday screen. This has the effect of normally making the CM evanescent between the antenna and the backwall. We have employed this code to obtain the antenna impedance due to the IBW and CM coupling with self-consistent ponderomotive force modifications of the density profile. Adding the sheath physics terms of Sec. IV C to the loading then gives rise to Fig. 10. The familiar rise at low power is due to sheath terms, whereas the sharp drop in loading at 200-400 kW is due to ponderomotively induced wave reflection at the LH layer. This model does not include any linear edge dissipation of the CM of the sort discusssed in Sec. IV B, so the true loading at 1 MW may be larger than the 0.5 ohms of the model.

We conclude that the low power loading seen in the experiment is consistent with the sheath effect on the CM, whereas ponderomotive effects enter at high power, $P_{rf} > 100$ kW, and act to reduce the coupling efficiency to the core plasma. As shown in Ref. 7 the density profile modifications are an important factor in increasing the power reflected into the CM. This interpretation is consistent with the experimentally observed changes in the edge density profile at high power.[1]

VI. Three-dimensional electromagnetic antenna modeling

The representation of the antenna geometry in the preceding sections has been made rather simplistic in order to render models which involve a minimal amount of computation effort. In this section, we supplement these models with full three-dimensional electromagnetic antenna modeling that was carried out with the High Frequency Structure Simulator (HFSS)[10] code. Two phaseable current straps were modeled (allowing 0-0 and 0-π phasing to simulate the 0-0-0-0 and 0-0-π-π cases of the experiment), with coaxial feeds and toroidal limiters. Three radial regions were employed in the simulations: a vacuum region at the antenna, followed by two radial regions to model lossy plasma. In each of these regions, a constant diagonal but anisotropic dielectric tensor ε was specified, with $\varepsilon_\perp = 1$ and $\varepsilon_\parallel = -a(1 + i \tan\delta)$, with $a > 0$. The constant a was chosen to be 100 and 400 respectively in the regions in front of the antenna, to simulate an increasing plasma density with large parallel conductivity, and the loss tangent was fixed at $\delta = 30°$ to model edge dissipation. More details of this modeling will be published separately.[11]

In Fig. 11, we show the code results for the poloidal dependence of the rf sheath driving voltage ($\int dz\, E_z$) in front of the antenna. The voltages have been scaled to 1 W of rf power, thus several kV of sheath voltage are expected at high power (1 MW). The two phasings show little difference in overall magnitude, suggesting that sheath power dissipation very close to the antenna (i.e. on the antenna Faraday shield or antenna bumper

limiters) is not a likely explanation for the high power phasing dependent loading that is observed in the experiments. In fact, for the IBW antenna geometry, the near field rf sheath-induced E×B convection[12] should tend to make the antenna-plasma interaction stronger in 0-π phasing, and this is not observed.

In addition to these near field calculations, the code can be run in a large simulation domain, where CM effects can be studied. In Fig. 12 we show contours of E_z in the y-z plane *near the main plasma boundary* for 0-0 and 0-π poloidal phasing. For this scaled run, dissipated power is 1 W per strap corresponding to a voltage drop per strap of about 10 V. It is evident that more field is present in 0-0 phasing, consistent with the faster radial evanescence of the CM in the 0-π case. Examination of the Poynting flux for these runs also suggests greater core heating efficiency in the 0-π case which is consistent with experimental observations. The reason is that E_z spreads faster toroidally for the 0-0 case, resulting in more toroidal power flow and therefore less radial flow into the plasma. However, the local dissipation in front of the antenna was found to be 50-70% larger in the 0-0 case, consistent with the higher loading that was measured experimentally.

VII. Discussion and summary

In this paper, we have explored a number of models for antenna coupling to the CM and ultimately the IBW. Each of the models has strengths and weaknesses; taken together, a coherent picture of the physics relevant to the TFTR experiments can be constructed. All three of the models of Sec. IV can explain the TFTR phasing dependence of R_L, which differs by about a factor of two between 0-0-0-0 and 0-0-π-π phasing. If there is a dissipation mechanism in the halo plasma, model 2 showed that it was possible to dissipate a substantial amount of power in the halo, and the amount depended on the reflection coefficient at the LH layer. It was shown in both model 3 and in the diffuse model of Sec. V that CM sheaths provide a likely explanation of the observed power dependence of R_L,

which differs by about a factor of two between the 1 kW and 1 MW power levels. Detailed three dimensional antenna modeling supports the critical idea of phasing dependent CMs, and further shows that the *heating efficiency* (as opposed to the loading) is largest in 0-0-π-π phasing, which is also consistent with experimental observations.

The main physical phenomena and mechanisms that emerge from this work are as follows. From previous studies, we know that steep density gradients imply that the launched EPW waves do not get into the plasma, but rather are reflected at the LH layer and can form standing CMs which further enhance the ponderomotive force. Thus coaxial mode formation and ponderomotive depletion (density profile modification) are synergistic in that CM can "dig its own well." The CM propagates for small k_y giving greater loading in phasings which accentuate this portion of the spectrum. Many dissipation mechanisms may exist for the CM in the halo plasma, but results appear to be insensitive to details. The CM is on the SW branch, therefore has $E_{||}$ and concomitant sheaths. These sheaths appear to explain the observed nonlinear dependence of R_L.

From the present studies, we conclude that the failure to efficiently couple power to the core plasma in the TFTR IBW experiments can be explained if the CM is launched and dissipated. Not much dissipation is needed if there is a lot of reflection at the LH layer. The present model is also not inconsistent with parasitic effects on the mode-transformed IBW in the SOL, as these effects would give $P_{core} < P_{out}$, and would not affect the interpretation of the loading given herein, because they are "far field" processes. The mechanism of coupling to coaxial modes is consistent with reflectometer observations in TFTR[2] that showed an rf signal on the high-field-side where the IBW itself was not expected.

Stepping back from the TFTR experiments, it is interesting to ask whether any unifying features can be gleaned from viewing the experimental successes and failures of IBW launch in the context of the present work. Perhaps the most sweeping statement one could make is that IBW heating has usually performed better in small rather than large

experiments. There may be a variety of factors for this (some more programmatic than fundamental) but it is interesting to note that large experiments often have large, relatively high density halo plasmas which should be more susceptible to CM propagation.

While the utility of an IBW in the core plasma for heating, current drive and other more exotic uses (such as α-channeling) provides strong motivation for continued work in IBW launch, the difficulty of coupling to such a short wavelength mode from relatively large hardware, such as a classical IBW antenna, is apparent. The strong nonlinearities inherent in coupling to an electrostatic mode with slow group velocity exasperates the situation. Perhaps fast-wave to IBW mode conversion schemes which avoid the IBW launch issue entirely may provide a practical solution to these difficulties. Alternatively, phaseable waveguide launchers (to reduce CM coupling) operating at high frequency (to mitigate ponderomotive effects) may merit investigation.

Acknowledgments

The authors wish to thank J.C. Hosea for discussions which motivated this work, and J.R. Wilson for helpful comments on the manuscript. Additionally, discussions with M. Carter, R. Majeski, R.I Pinsker and M. Ono are gratefully acknowledged. This work was supported by the U.S. Department of Energy under grant numbers DE-FG03-97ER54392, DE-FG03-93ER54212, DE-AC02-76CH03073, DE-FG02-96ER5438 and by sub-contract number S-04074-F with Princeton Plasma Physics Laboratory; however, this support does not constitute an endorsement by DOE or PPPL of the views expressed herein.

Appendix A: Energy conservation theorem and power split

It is straightforward to show from the general statement of Poynting's theorem that the antenna loading power P_{load} is equal to the Poynting flux radiated by the antenna. In

order to derive the split of this power in the model geometry of Fig. 3 into "outgoing" power (i.e. power radiated to $x < 0$) and power dissipated in the halo plasma,

$$P_{load} = P_{out} + P_{halo}, \tag{A1}$$

we evaluate the Poynting flux at $x = 0$ explicitly to obtain P_{out}, and take P_{halo} to be the remaining portion of P_{load}. We shall illustrate the power split calculation in the capacitive coupling limit because an explicit evaluation of P_{out} in the inductive coupling limit ($G = 1$) requires both an explicit feeder model and extensions to Eq. (7). [The second order SW limit of Eq. (7) gives reliable expressions for Φ and the loading, but not the rf magnetic fields required for the Poynting flux calculation.]

We first show how the jump in radial Poynting flux S_x across the current strap is related to P_{load}. Employing [...] to denote a jump across the current strap

$$[S_x] = \frac{-c}{16\pi} E_z^* [B_y] + cc = \frac{-1}{4L_y} E_{za}(k_{||}) I_k^* + cc \tag{A2}$$

where cc denotes complex conjugate, and $[B_y] = 4\pi I_k / cL_y$ has been used. The power is obtained from S_x as $P = L_y \int dz\, S_x(z) = L_y \int (dk_{||}/2\pi)\, S_x(k_{||})$. But $P_{load} = I_0^2\, Re(Z) / 2$ where Z is obtained from Eq. (15), demonstrating the energy conservation theorem explicitly.

When there is dissipation in the halo, the S_x delivered to $x = 0$ will be reduced from its value at the current strap. Calculating P_{out} from $S_x(x=0)$ explicitly, we have

$$P_{out} = -L_y \int \frac{dk_{||}}{2\pi} S_x(k_{||}) = \frac{\omega L_y}{16\pi^2} \int dk_{||}\, |A|^2\, k_r\, (1-\alpha^2), \tag{A3}$$

where we have taken the limit $n_{||} >> 1$ and employed $E_z \approx -ik_{||}\Phi$, $B_y \approx -(\varepsilon_\perp / n_{||}) \partial\Phi/\partial x$. On substituting A from Eq. (11) with $G \approx -n_{||}^2$ we find

$$P_{out} = \frac{2I_0^2(1-\alpha^2)}{\omega L_y} \int_{-\infty}^{\infty} dk_{||}\, \frac{(1-\cos k_{||} L_z) k_r}{|\exp(ika) + \alpha \exp(-ika)|^2\, |\cot(ks) + iQ|^2\, |k|^2}. \tag{A4}$$

Similarly, it is possible to calculate the total left-going power flow just to the left of the current strap, and the right-going power flow just to the right of the current strap. The

latter P_{halo+} represents dissipation between the current strap and the backwall, while the former includes P_{out} as well as P_{halo-}, the dissipation between the current strap and x = 0. We obtain

$$P_{halo+} = \frac{I_0^2}{\omega L_y} \int_{-\infty}^{\infty} dk_{\|} \frac{(1-\cos k_{\|} L_z)[k_i \sin(2k_r s) - k_r \sinh(2k_i s)]}{|\sin(ks)|^2 \, |\cot(ks)+iQ|^2 \, |k|^2}, \tag{A5}$$

$$P_{halo-} = \frac{2I_0^2}{\omega L_y} \int_{-\infty}^{\infty} dk_{\|} \frac{(1-\cos k_{\|} L_z) h_{halo-}}{a \, |\exp(ika)+\alpha \exp(-ika)|^2 \, |\cot(ks)+iQ|^2 \, |k|^2}. \tag{A6}$$

where h_{halo-} is given by Eq. (26). It is also possible to show explicitly that $P_{load} = P_{out} + P_{halo+} + P_{halo-}$. Details will be omitted, but it is useful to note that Re(Z) can be written in the form

$$Re(Z) = \frac{-4}{\omega L_y} \int_{-\infty}^{\infty} dk_{\|} \frac{(1-\cos k_{\|} L_z) Im[k^*[\cot(k^* s) - iQ^*]]}{|\cot(ks)+iQ|^2 \, |k|^2}, \tag{A7}$$

where the $k^* \cot(k^* s)$ term gives rise to P_{halo+}, and the $k^* Q^*$ term gives rise to $P_{halo-} + P_{out}$.

As noted in the main text, the capacitive limit is not the most realistic one for IBW antenna modeling. The inductive (G = 1) forms of the power split are obtained from the above, by multiplying the integrands for P_{load}, P_{out}, P_{halo+} and P_{halo-} by $1/n_{\|}^2$, to yield Eqs. (24) - (26).

Appendix B: Sheath voltages

The sheath voltage may be calculated from Eq. (19) by expressing $E_z(k_{\|})$ in terms of Φ_{ka} and inverting the Fourier transform. Noting that Re(k) > 0 is chosen by convention for both signs of $k_{\|}$, the parity of the Fourier transform integral may be exploited to obtain

$$\Phi(x, z') = \frac{-8iI_0\omega}{c^2 L_y} \int_0^\infty \frac{dk_\parallel}{k_\parallel^2} \sin\left(\frac{k_\parallel L_z}{2}\right) \frac{\sin(k_\parallel z')}{k[\cot(ks)+iQ]} X(x), \tag{B1}$$

where $z' = z - L_z/2$, and $X(x)$ gives the radial dependence

$$X(x) = \begin{cases} \dfrac{\exp(ikx) + \alpha\exp(-ikx)}{\exp(ika) + \alpha\exp(-ika)}, & 0 < x < a \\ \dfrac{\sin[k(g-x)]}{\sin(ks)}, & a < x < g \end{cases} \tag{B2}$$

The sheath voltage drop along a given field line is $\Phi(x, \infty) \equiv \Phi_\infty(x)$. The asymptotic evaluation of the integral for large z' is accomplished by noting that the $\sin(k_\parallel z')$ term oscillates rapidly, forcing the dominant contribution to the integral to arise from small $k_\parallel$. Thus, the remaining terms in the integral may be expanded about $k_\parallel = 0$, resulting in

$$\Phi_\infty(x) = \frac{-2\pi i I_0 \omega L_z}{c^2 L_y k_y [\coth(k_y s)+Q_y]} X_0(x), \tag{B3}$$

where $X_0(x)$ is the $k_\parallel = 0$ limit of $X(x)$,

$$X_0(x) = \begin{cases} \dfrac{\exp(k_y x) + \alpha\exp(-k_y x)}{\exp(k_y a) + \alpha\exp(-k_y a)}, & 0 < x < a \\ \dfrac{\sinh[k_y(g-x)]}{\sinh(k_y s)}, & a < x < g \end{cases} \tag{B4}$$

Finally, we define the radially averaged sheath voltage by integration of Eq. (B3) over all x as

$$\langle V_{sh} \rangle = \langle \Phi_\infty(x) \rangle \tag{B5}$$

where everything except $X_0(x)$ pulls through the average, and $\langle X_0 \rangle$ is given by Eq. (30). The power dissipation from these halo sheaths is then obtained by a straightforward application of Eq. (20).

In addition to the halo sheaths, power dissipation from the evanescent tail of the CM, extending into the region $x < 0$, may be calculated, although it requires a slight

embellishment to the eigenfunction of Eqs. (10) - (12). In region 1, Φ given by Eq. (9b) can be decomposed into standing wave and outgoing wave pieces as

$$\Phi = A[-2i\alpha \sin(kx) + (1+\alpha)\exp(ikx)]. \tag{B6}$$

The outgoing piece $(1+\alpha)\exp(ikx)$ is irrelevant to tail sheaths. (It mode converts to the IBW, and may form IBW sheaths, but these are not treated here.) Consequently, the exponential tail of the CM is obtained by considering the matching problem

$$\Phi(x>0) = -2i\alpha A \sin(kx+\delta) \tag{B7}$$

onto an evanescent tail of the form

$$\Phi(x<0) = F \exp(\kappa x) \tag{B8}$$

where F is to be determined and κ (> 0 by convention) is the (evanescent) root of the dispersion relation, Eq. (6). The SW matching conditions in the limit $n_{||}^2 > \varepsilon_\perp$ are continuity of Φ and $\varepsilon_\perp \partial\Phi/\partial x$. The matching procedure yields $\varepsilon_\perp \kappa = k \cot\delta$, which gives $\delta << 1$ for a high density (large $|\varepsilon_\perp|$) plasma in the region $x < 0$ (as assumed previously). Employing $F = -2i\alpha A\, k/(\kappa\varepsilon_\perp)$ we can form $\Phi(x, z')$ analogous to Eq. (B1) and take the limit $z' \to \infty$. In this case, for $k_{||} \to 0$, one must retain the electromagnetic skin term, which results in $\kappa \to \delta_e^{-1} = \omega_{pe}/c$ (or else $\kappa \to 0$ as $k_{||} \to 0$). Equation (B3) is recovered with the replacement

$$iX_0(x) \to X_{0t}(x) = \frac{-2i\alpha \exp(x/\delta_e)\, k_y\, \delta_e}{\varepsilon_\perp[\exp(k_y a)+\alpha \exp(-k_y a)]} \tag{B9}$$

Finally, performing the radial integral results in Eq. (31).

References

1. J.R. Wilson, R.E. Bell, S. Bernabei, K. Hill, J.C. Hosea, B. LeBlanc, R. Majeski, R. Nazikian, M. Ono, C.K. Phillips, G. Schilling, S. von Goeler, C.E. Bush and G.R. Hanson, Phys. Plasmas **5**, 1721 (1998).
2. J. H. Rogers, R.E. Bell, S. Bernabei, J.C. Hosea, B. LeBlanc, R. Majeski, R. Nazikian, M. Ono, C.K. Phillips, G. Schilling, J.R. Wilson, C.E. Bush, D.A. D'Ippolito, G.R. Hanson and J.R. Myra, in *AIP Conference Proceedings 403 - Radio Frequency Power in Plasmas,* Savannah, GA (American Institute of Physics, New York, 1997), p. 13.
3. M. Ono, Phys. Fluids B **5**, 241 (1993); and refs. therein.
4. H. Biglari, M. Ono, P.H. Diamond and G.C. Craddock, in *AIP Conference Proceedings 244 - Radio Frequency Power in Plasmas,* Charleston SC, USA (American Institute of Physics, New York, 1992), p. 376.
5. B. LeBlanc, M. Ono, W. Tighe, J. Dunlap, R. Bell, T.K. Chu, A. England, R. Isler, S. Kaye, D. McCune, M. Okabayashi, A. Post-Zwicker, H. Takahashi and S. Sesnic, in *AIP Conference Proceedings 289 - Radio Frequency Power in Plasmas,* Boston, MA (American Institute of Physics, New York, 1994), p. 68
6. D.A. D'Ippolito, J.R. Myra, M. Bures, and J. Jacquinot, Plasma Phys. Cont. Fusion **33**, 607 (1991); and refs. therein.
7. D.A. Russell, J.R. Myra and D.A. D'Ippolito, Phys. Plasmas **5**, 743 (1998).
8. J.R. Myra, D.A. D'Ippolito, D.A. Russell, and J.H. Rogers in *AIP Conference Proceedings 403 - Radio Frequency Power in Plasmas,* Savannah, GA (American Institute of Physics, New York, 1997), p. 459.
9. D.A. D'Ippolito and J.R. Myra, Phys. Plasmas **3**, 420 (1996).
10. Hewlett-Packard Company, http://www.hp.com/.
11. T. Intrator, private communication, 1997.
12. D.A. D'Ippolito, J.R. Myra, J. Jacquinot and M. Bures, Phys. Fluids B **5**, 3603 (1993).

Tables

Table I. Parameters for the numerical results of Sec. IV, unless otherwise stated.

halo	
T_e (eV)	2.9
μ (amu)	2
n_e (cm^{-3})	3×10^9
A (cm^2)	4000
f (MHz)	75
g (cm)	20
L_z (cm)	65
L_y (cm)	60
a (cm)	5
SOL	
α	-0.9
n_e (cm^{-3})	3×10^{11}

Figure Captions

1. TFTR data for loading vs. antenna location for 0-0-0-0 and 0-0-π-π poloidal phasing.
2. TFTR data for loading vs. rf power in 0-0-π-π phasing.
3. Model geometry for the analytical coaxial mode loading calculations. The coaxial mode is an electron plasma wave trapped in the halo plasma between the lower hybrid resonance (LHR) layer and the vessel backwall. The halo is treated as a uniform density plasma in regions 1 and 2.
4. Normalized loading vs. k_y for model 1. Purely outgoing BC ($\alpha = 0$) and mostly reflecting BC ($\alpha = -0.9$) cases are shown.
5. Normalized loading vs. n_e for model 1. Two different values of k_y are shown, corresponding to the dominant spectral peaks in 0-0-0-0 and 0-0-π-π- phasing.
6. Normalized loading vs. α for model 1 and two values of k_y.
7. Normalized total loading vs. k_y (upper), and portion thereof (lower) due to power dissipation in the halo for model 2. Parameters are $\alpha = 0$ and $k_d = 0.93$.
8. Normalized total loading vs. P_{rf} for model 3. For these curves $\alpha = -0.9$ and the cases $k_y g = 0$ and 3 are illustrated. For each k_y, the upper (solid) curve gives the total loading, and the lower (dashed) curve gives the portion thereof due to sheath dissipation in the halo and tail.
9. Sheath saturation current I_{sat} vs. k_y for model 3. The upper curve is the total saturation current; contributions from the halo and tail sheaths are indicated.
10. Loading vs. P_{rf} for $k_y = 0$ with self-consistent ponderomotive force and density profile modifications. Shown is the total loading (upper) and portion thereof (lower) due to the launched IBW waves.
11. Sheath voltage V_{sh} vs. poloidal distance y as computed from three dimensional antenna modeling by the HFSS code.

12. Contours of E_z in the y-z plane for (a) 0-0 and (b) 0-π poloidal phasing. Results shown are from three dimensional antenna modeling by the HFSS code, and correspond to 1 Watt power dissipation per strap. Feed positions for each strap are indicated, the other end of the straps are grounded. Bold contours correspond to negative fields, $E_z < 0$.

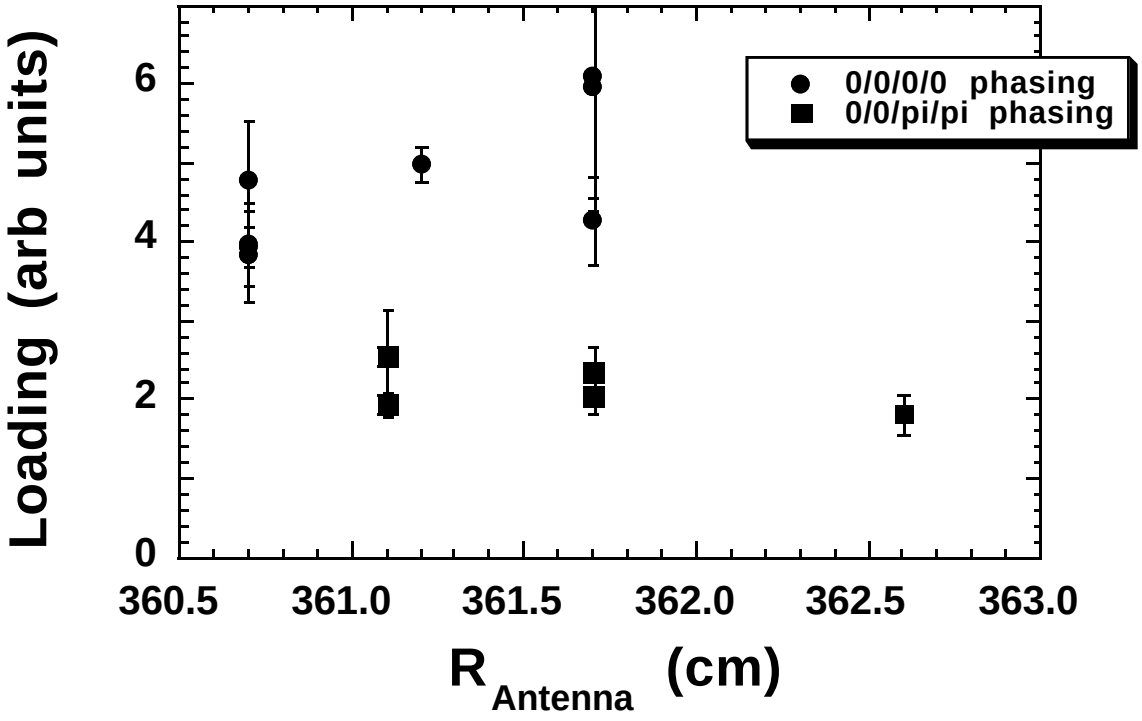

Fig. 1. TFTR data for loading vs. antenna location for 0-0-0-0 and 0-0-π-π poloidal phasing.

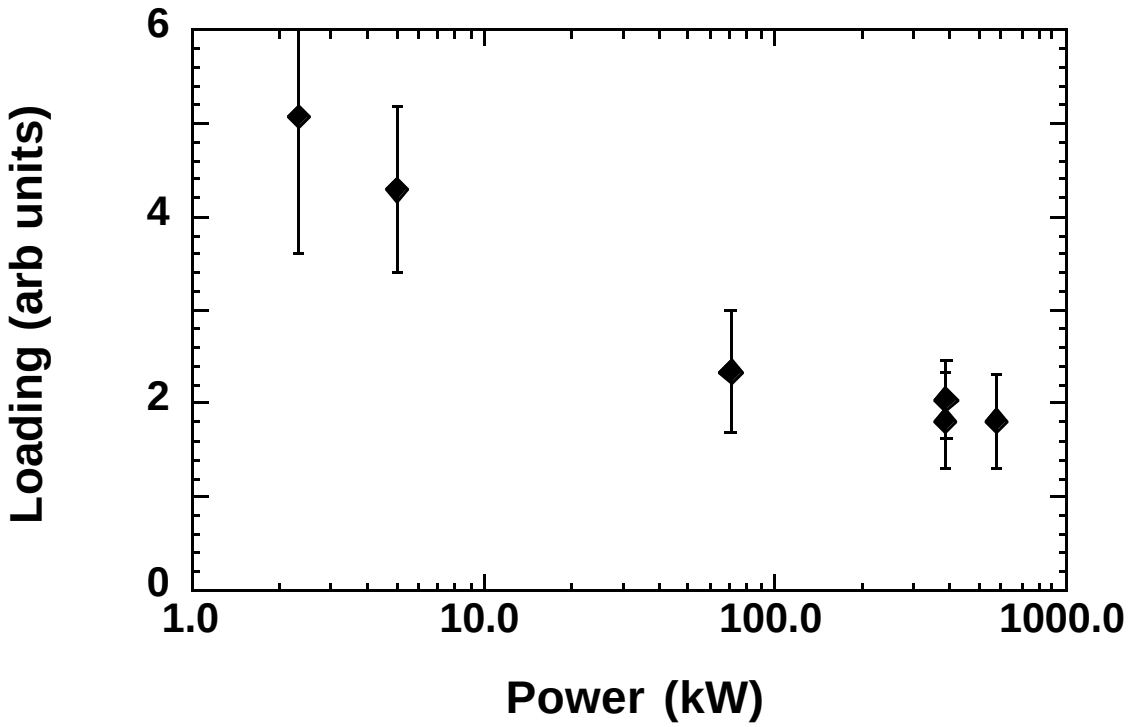

Fig. 2. TFTR data for loading vs. rf power in 0 0-π-π phasing.

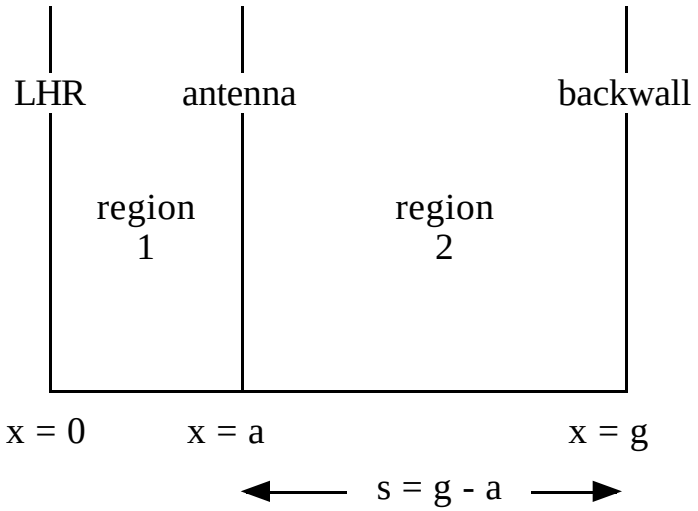

Fig. 3. Model geometry for the analytical coaxial mode loading calculations. The coaxial mode is an electron plasma wave trapped in the halo plasma between the lower hybrid resonance (LHR) layer and the vessel backwall. The halo is treated as a uniform density plasma in regions 1 and 2.

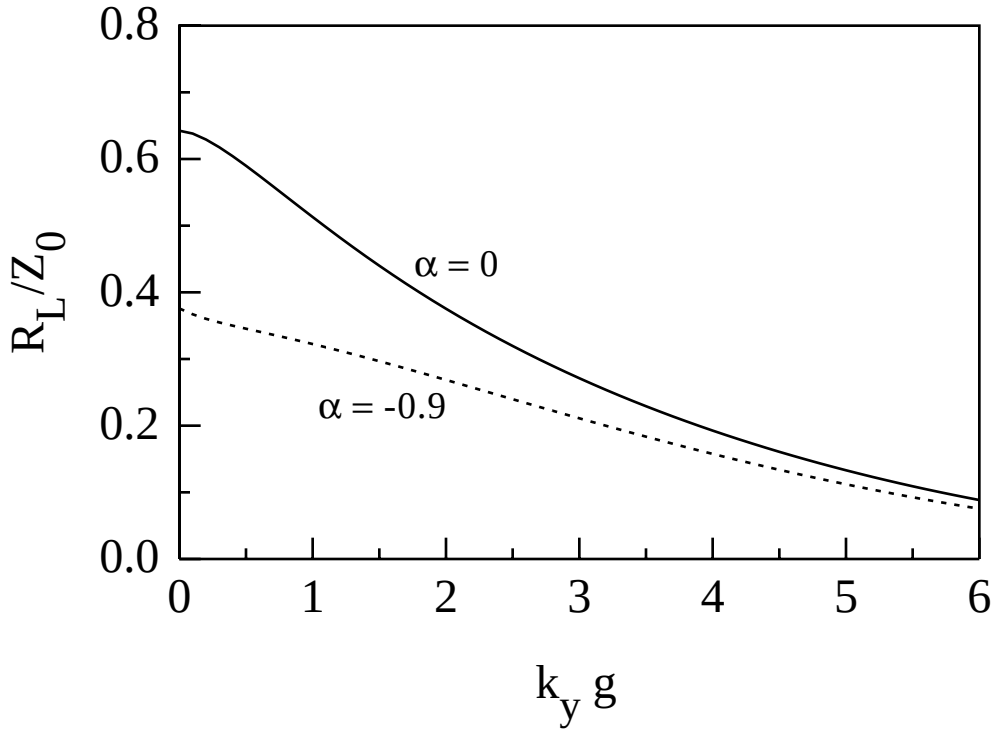

Fig. 4. Normalized loading vs. k_y for model 1. Purely outgoing BC ($\alpha = 0$) and mostly reflecting BC ($\alpha = -0.9$) cases are shown.

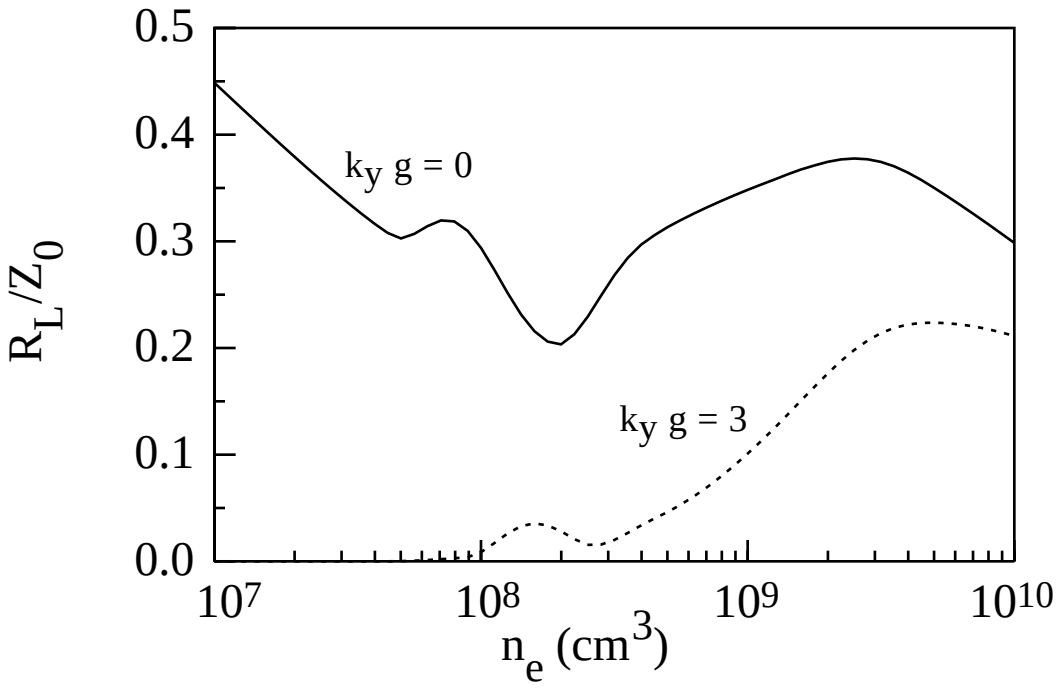

Fig. 5. Normalized loading vs. n_e for model 1. Two different values of k_y are shown, corresponding to the dominant spectral peaks in 0-0-0-0 and 0-0-π-π- phasing.

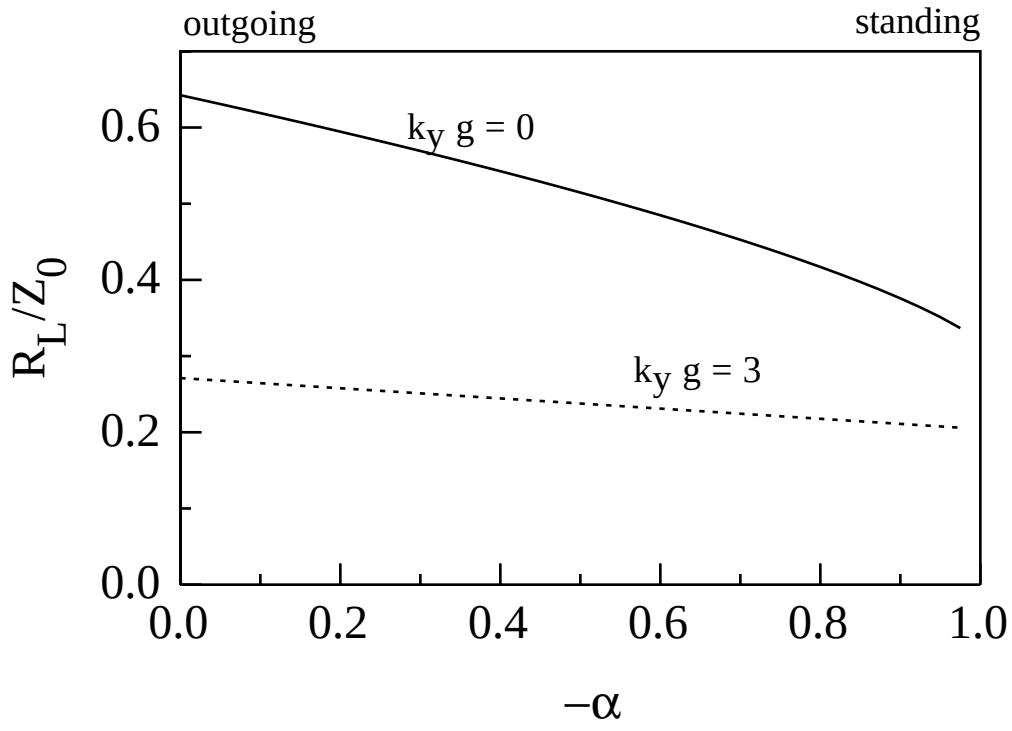

Fig. 6. Normalized loading vs. α for model 1 and two values of k_y.

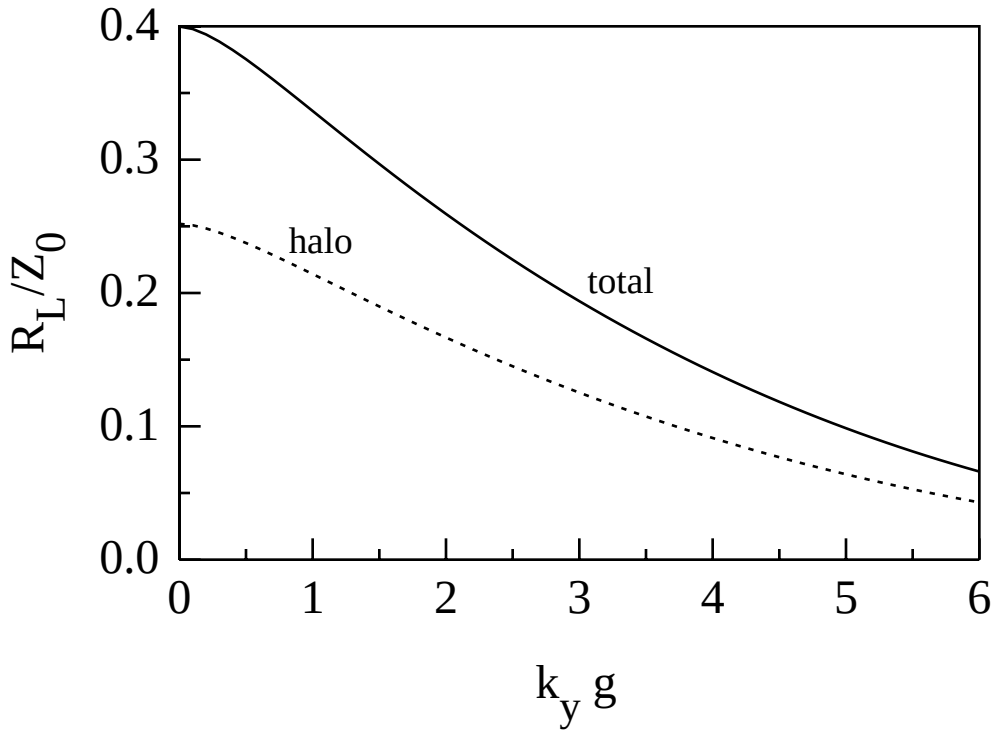

Fig. 7. Normalized total loading vs. k_y (upper), and portion thereof (lower) due to power dissipation in the halo for model 2. Parameters are $\alpha = 0$ and $k_d = 0.93$.

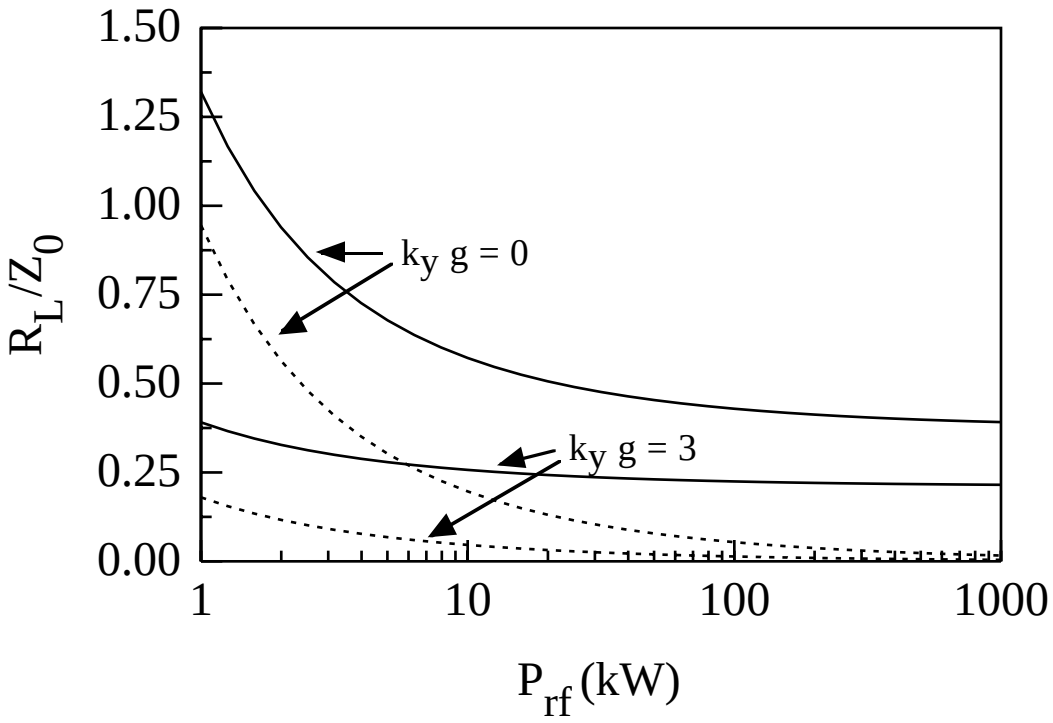

Fig. 8. Normalized total loading vs. P_{rf} for model 3. For these curves α = –0.9 and the cases $k_y g$ = 0 and 3 are illustrated. For each k_y, the upper (solid) curve gives the total loading, and the lower (dashed) curve gives the portion thereof due to sheath dissipation in the halo and tail.

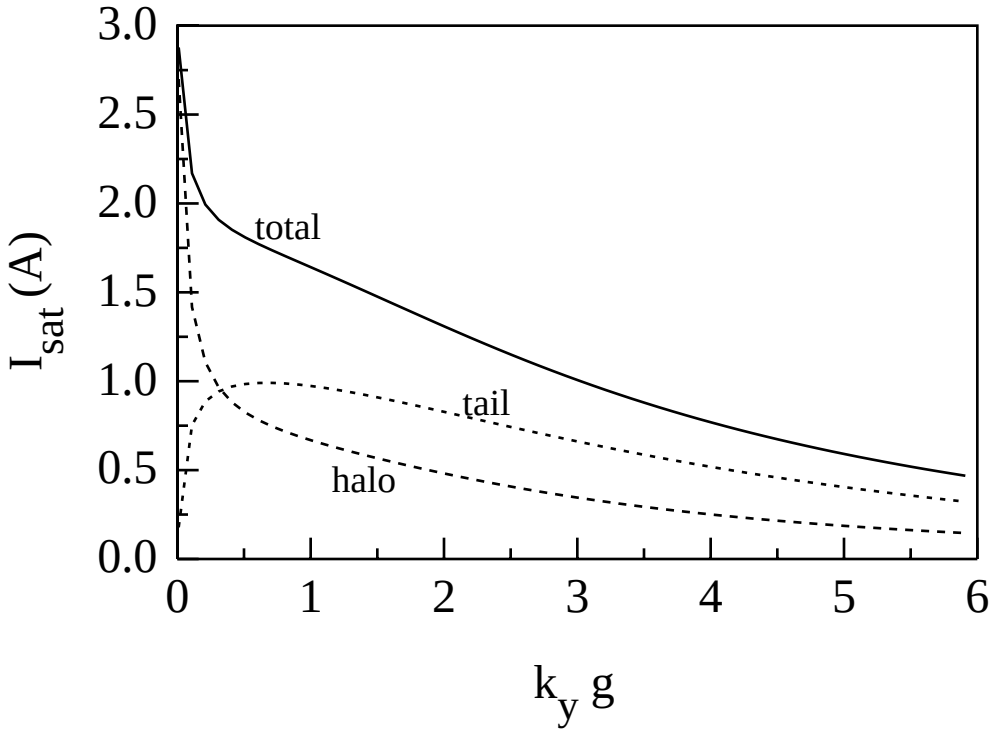

Fig. 9. Sheath saturation current I_{sat} vs. k_y for model 3. The upper curve is the total saturation current; contributions from the halo and tail sheaths are indicated.

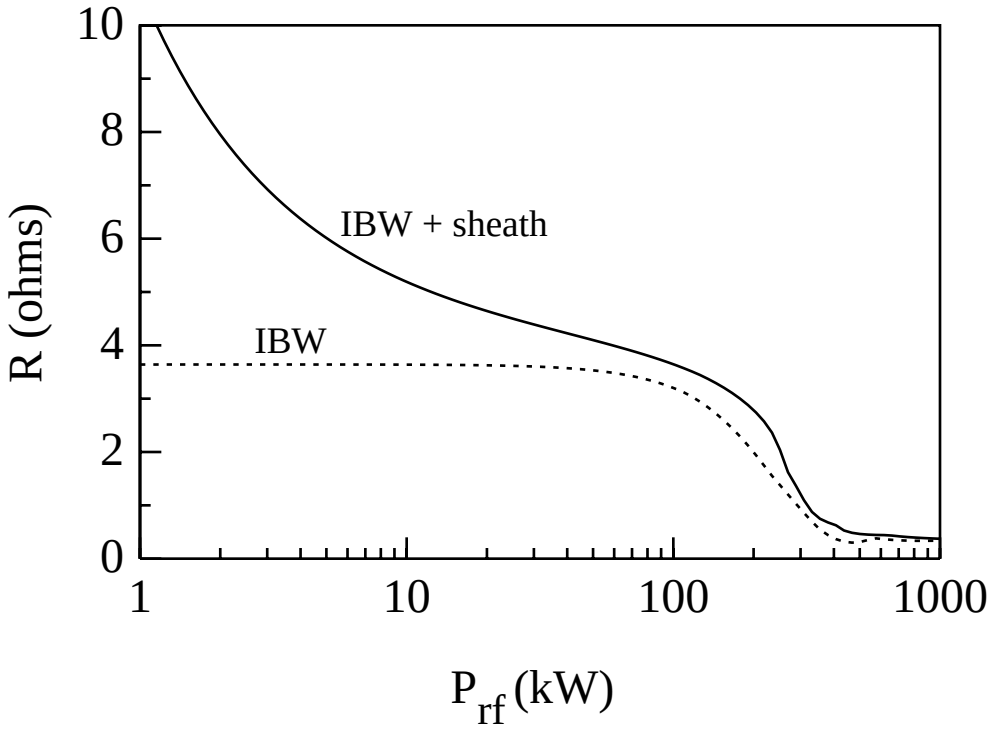

Fig. 10. Loading vs. P_{rf} for $k_y = 0$ with self-consistent ponderomotive force and density profile modifications. Shown is the total loading (upper) and portion thereof (lower) due to the launched IBW waves.

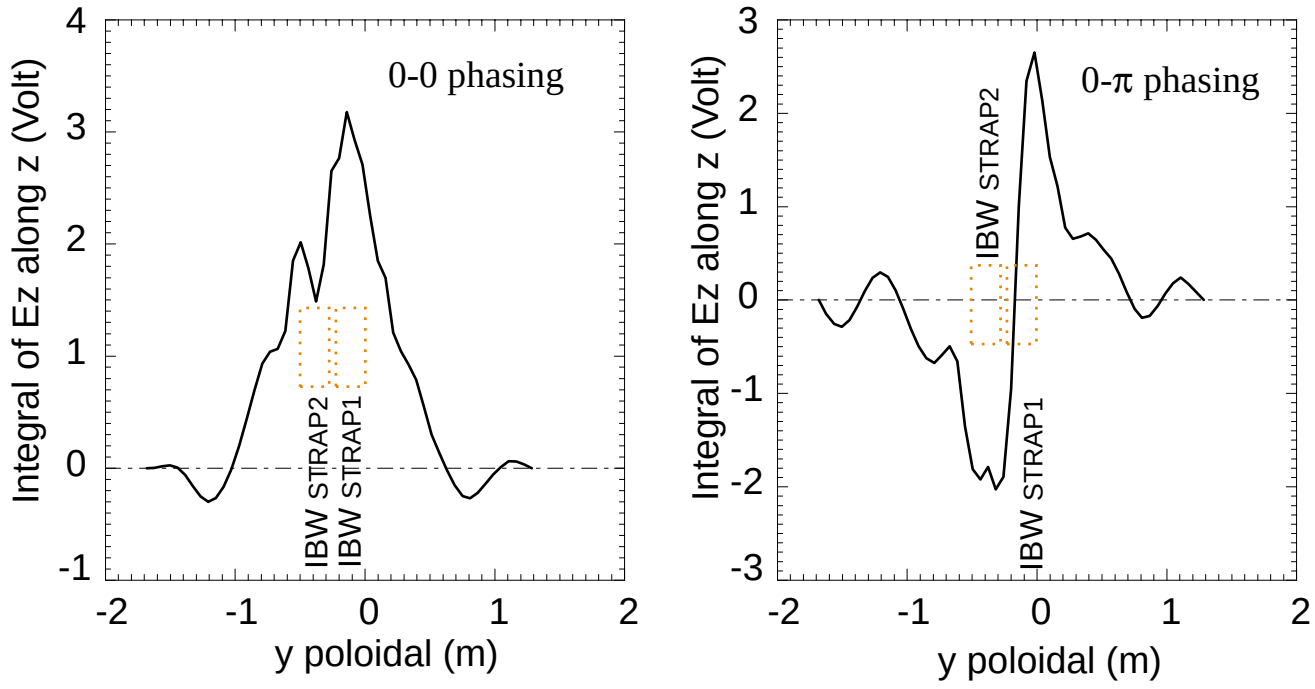

Fig. 11. Sheath voltage V_{sh} vs. poloidal distance y as computed from three dimensional antenna modeling by the HFSS code.

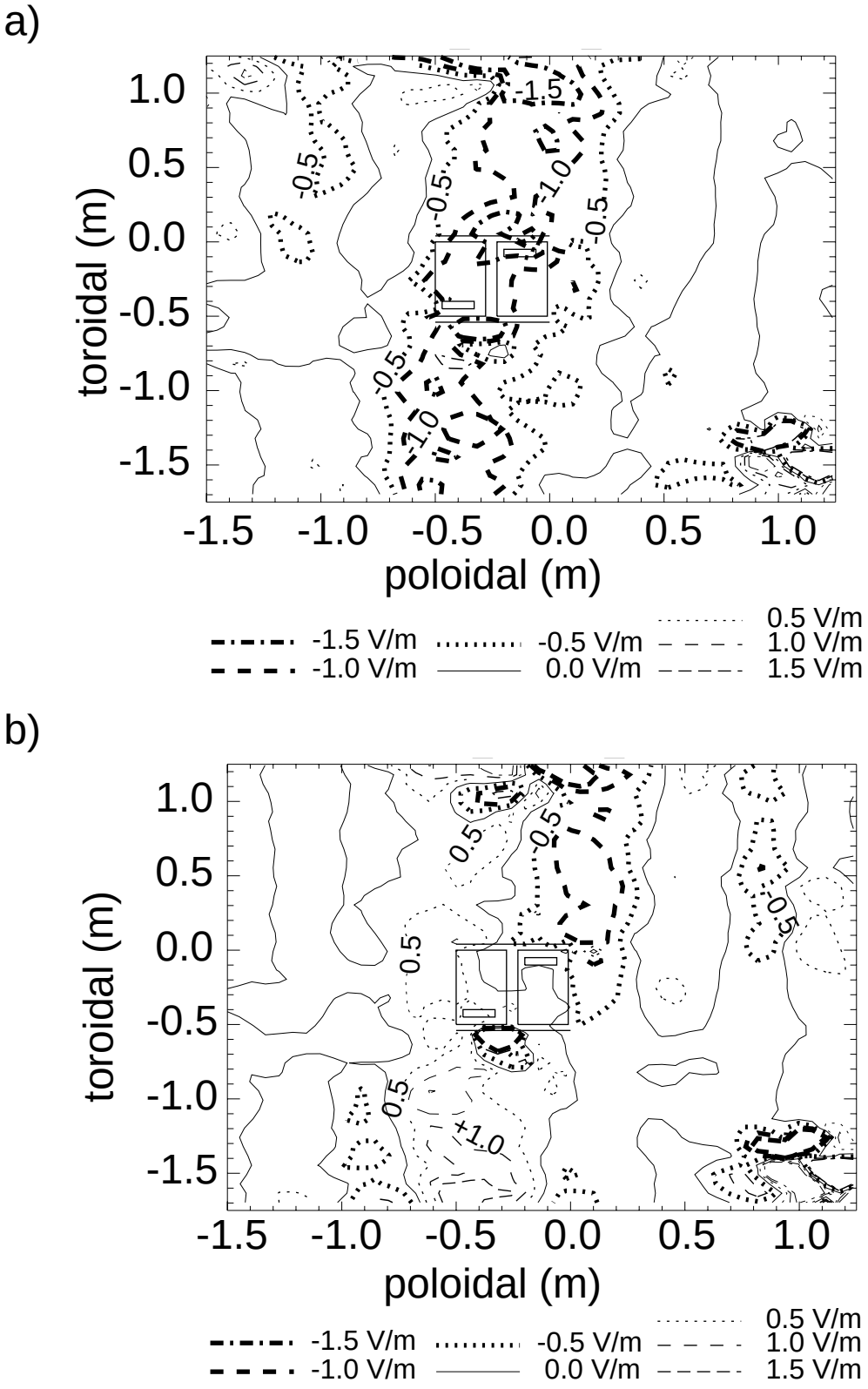

Fig. 12. Contours of Ez in the y-z plane for (a) 0-0 and (b) 0-π poloidal phasing. Results shown are from three dimensional antenna modeling by the HFSS code, and correspond to 1 Watt power dissipation per strap. Feed positions for each strap are indicated, the other end of the straps are grounded. Bold contours correspond to negative fields, Ez < 0.